BULLETIN OF THE POLISH ACADEMY OF SCIENCES
TECHNICAL SCIENCES, Vol. 70(2), 2022, Article number: e140692
DOI: 10.24425/bpasts.2022.140692

An improved air supply scheme for battery energy storage systems

Zhu XINLONG[1], Shi HONG[1]*, Xu WENBING[1], Zhang TONG[2], and Wang YANSONG[2]

[1] College of Energy & Power Engineering, Jiangsu University of Science and Technology, Mengxi, Jingkou, Zhenjiang 212003, China
[2] Key Laboratory of Aircraft environment control and life support, MIIT, Nanjing University of Aeronautics & Astronautics, Yudao Street, Nanjing 210016, China

Abstract. The overall efficiency of battery energy storage systems (BESSs) strongly depends on the temperature uniformity of the batteries, usually disregarded in studies of the integrated performance of BESSs. This paper presents a new battery thermal management system (BTMS) using a personalized air supply instead of a central air supply. Thermal models are established to predict the thermal behavior of BESSs with 400 battery packs. Moreover, several optimizations comprising the effect of the position and number of air inlets, the number, and angle of the baffles on the air distribution in the ducts are proposed. The results show that the distributed air supply from the main air inlet makes the air velocity in the main air ducts more uniform. It is demonstrated that air deflection is the main source of airflow inhomogeneity at the air outlets. The airflow uniformity is better when the baffles are added at the entrance and the bottom of each riser duct than at other locations. The improved air supply scheme makes the nonuniformity coefficient of air velocity reduced from 1.358 to 0.257. The findings can guide the selection of a cooling form to enhance the safety of BESSs.

Key words: battery energy storage systems; air cooling duct; baffles.

1. INTRODUCTION

Battery energy storage systems (BESSs) provide a new solution to the imbalance between the supply and demand of power systems caused by the peak–valley difference of power consumption [1]. In recent years, BESSs have been used in many large-scale projects [2]. During the charging and discharging of BESSs, its batteries will produce a significant amount of heat. Because there are more than 5 000 batteries in the energy storage system [3], the batteries are arranged closely, and the heat generated will not dissipate quickly. The accumulated heat will cause temperature differences among the batteries [4]. In the long-term operation of the batteries, serious inconsistencies will arise in the internal resistances and capacities of the batteries, leading to reduced cycle life, thermal runaways, and even fires or explosions [5–7]. Therefore, the performance of BESSs is closely related to the temperature and its uniformity, the optimal temperature of the battery is similar to the temperature that is comfortable to a human body [8, 9].

Many researchers proposed cooling optimization strategies aimed at improving thermal performances [10–13]. Forced air cooling systems are a preferred option due to their high reliability, low manufacturing cost, and simple structure and layout [14–17].

Zhang *et al*. [18] proposed that the cooling air was first sent to the wind wall of the container energy storage system through the duct, and then it was distributed to the battery packs through a series of holes in the wind wall. Wang *et al*. [19] inserted tapered and divergent baffles in the cooling duct of a battery pack. They used fans to adjust the airflow and reduce the vortex. Wang *et al*. [20] installed baffles in the air ducts to make the airflow and temperature fields uniform. Sun *et al*. [21] found that the most uniform air distribution is obtained inside a Z-shaped cooling channel, in which the maximum temperature difference among the batteries was considerably low. Lu *et al*. [22] designed a "U-type" cooling channel and the maximum temperature difference among the batteries was lower by 3 K. Additionally, Liu *et al*. [23] proposed an innovative "J-type" cooling channel for BTMSs by strategically combining "U-type" and "Z-type" designs. This optimal control strategy was also developed to improve system temperature uniformity. Hba *et al*. [24] designed a scheme of adding a heat pipe made of copper sheets to the air-cooling system. The heat pipe reduced the battery surface temperature by more than 40%. Huang *et al*. [25] proposed a new BTMS based on forced-air convection cooling that used PCMs and fins. The fins improved the thermal conductivity of the PCMs and expanded the surface area of the heat exchanger. The maximum temperature and maximum temperature difference of the optimized BTMS were lower than those of a standard BTMS by 38.72% and 40.09%, respectively. However, both in experimental and theoretical publications, the BESSs auxiliary consumption and compact structural design are often neglected. Problems, such as excessive cooling of the supplied air, unevenness of the air supply, complex structures, and high resistance characteristics of the air ducts, still exist.

This paper proposes an improved air supply scheme for BESSs based on the concept of equipment comfort and compact

*e-mail: shihong@nuaa.edu.cn

Manuscript submitted 2021-08-01, revised 2021-08-01, initially accepted for publication 2022-01-26, published in April 2022.

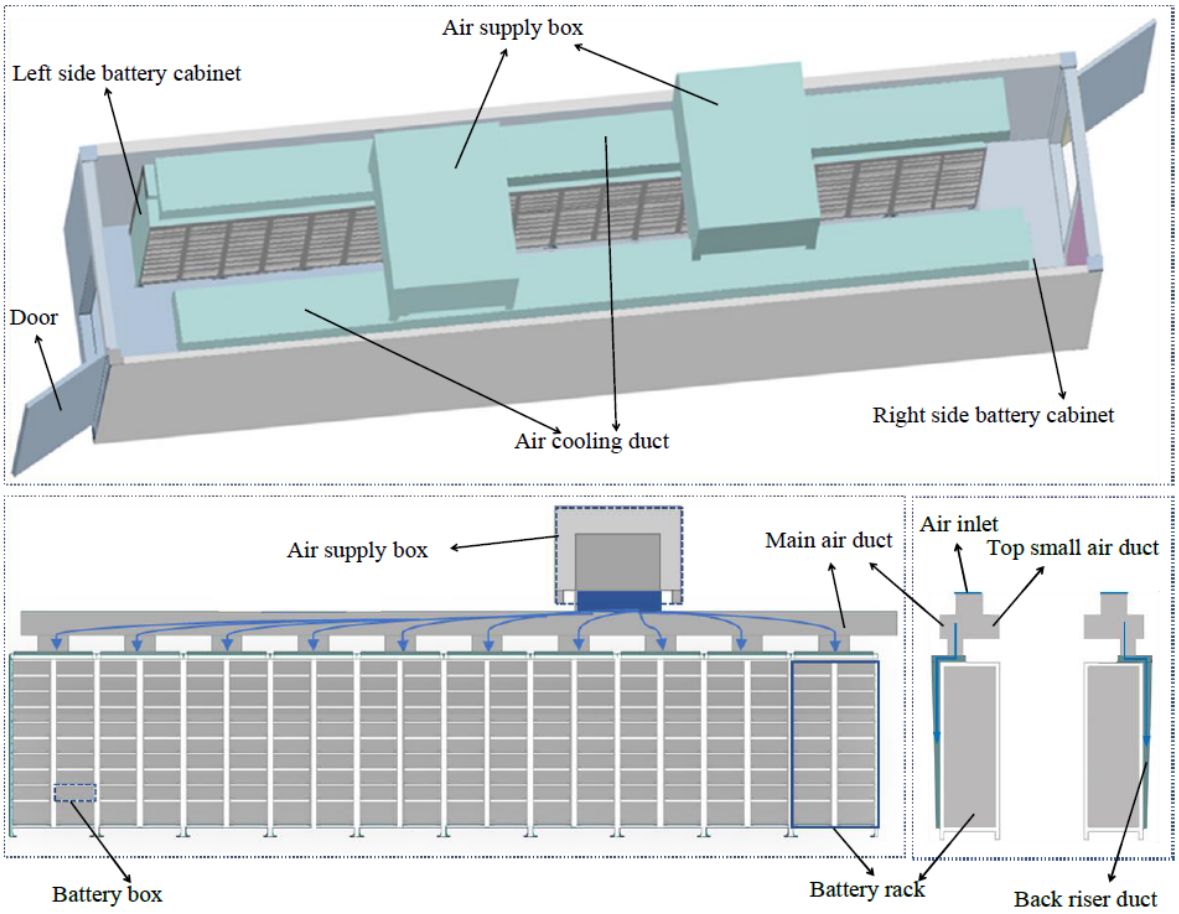

Fig. 1. Battery pack layout and air-cooling duct design

design. The air distribution performances of different airflow ducts are investigated by computational fluid dynamics. Then, the structure of the air-cooling duct is optimized by changing the form of air inlets and adding baffles in some key locations. The results offer a reference for air supply duct mode choosing.

2. AIR COOLING DUST STRUCTURE

As shown in Fig. 1, the two battery cabinet sets are symmetrically placed in the battery container. In each battery cabinet, there are ten battery racks provided with two rows of battery packs and each row has ten stacked battery packs. Initially, each air supply box is responsible for each side of the battery cabinet. The path followed by the airflow is as follows: air inlet → main air duct → small air duct at the top → riser duct at the back → battery pack.

3. NUMERICAL COMPUTATION METHODOLOGY

3.1. Mesh division

Because the ducts on both sides of the container are symmetrical, only one side is selected as the research object. The duct is modeled and divided into a structural grid by ICEM 18.0 software, as is shown in Figs. 2 and 3. The ducts are numbered from 1 to 20 starting from the left, and the outlets are numbered from 1 to 10 starting from the top.

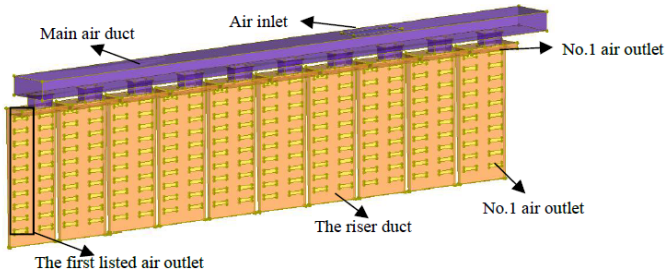

Fig. 2. Air cooling duct model

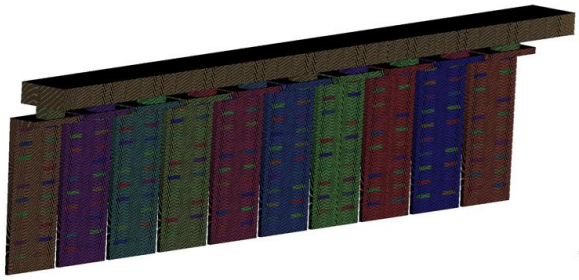

Fig. 3. Air cooling duct mesh model

3.2. Boundary condition of the air-cooling duct

Boundary conditions, which are set as realistically as possible, are presented in Table 1. The SST k–ω turbulence model is selected, and the SIMPLE algorithm is used to simulate the airflow field in the cooling duct.

Table 1
Boundary conditions of the air-cooling duct

Part	Parameters	Value
Air inlet	Velocity-inlet	15.76 m/s
Air outlet	Pressure-outlet	0 Pa
Wall	Wall	insulation

3.3. Mesh validation

To verify grid independence, the average air velocity at the outlet of a riser duct is selected as the evaluation index. Five sets of grids are compared in Table 2.

Table 2
Grid independence verification

Number of the grid (million)	Average air outlet velocity of a riser duct (m/s)
2.9	1.57986
3.4	1.62546
3.9	1.63826
4.4	1.64395
4.9	1.64278

As shown in Table 2, when the number of grids exceeds 4.4 million, the average air velocity tends to be constant. Therefore, 4.4 million is chosen as the number of grids in the duct model.

3.4. Algorithm verification

The model used by Yao *et al*. is taken as the verification example [26]. The cooling ventilation ducts of offshore platforms are used to solve the heat dissipation problem of engines and transformers, which is shown in Fig. 4.

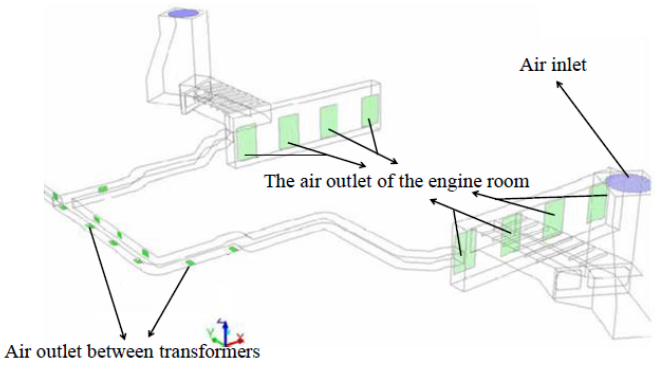

Fig. 4. Duct model used by Yao *et al*. [26]

The comparison of numerically simulated resistances and measured resistances is shown in Table 3.

Table 3
Comparison of numerically simulated resistances and measured resistances

Working condition	1	2	3	4	5	6
Ventilation rate (10^4 m^3/h)	15	16	17	18	19	20
Numerical simulation of resistance value (Pa)	916.8	1042.5	1178.7	1320.0	1471.2	1632.6
Actual measured resistance value (Pa)	913.5	1037.8	1170.2	1313.8	1463.4	1623.8

4. CALCULATION RESULTS AND ANALYSIS

4.1. Simulation analysis of the initial scheme of the air-cooling duct

The normal air velocity at each outlet is numerically calculated (Tables 4 and 5).

It can be seen from Tables 4 and 5 that significant differences exist among the air velocities at the different outlets. Excessive air supply at the bottom outlet and serious reversed flow phenomenon occurs in some locations.

The uniformity of air velocity at each outlet is evaluated using the coefficient of nonuniformity of air velocity. Formula (1) defines the coefficient of air velocity nonuniformity:

$$S = \frac{\sqrt{\frac{1}{m}\sum (V_i - \overline{V})^2}}{\overline{V}}, \tag{1}$$

where S is the nonuniformity coefficient of air velocity, V_i is the air velocity at the i-th outlet, $\overline{V}$ is the average value of the air velocity at the outlets, and m is the number of air outlets.

According to Formula (1), S of the initial scheme of the air-cooling ducts is 1.358, which is found to be large. In order to find the cause of nonuniform airflow inconsistency, the distribution of the airflow field in the duct is analyzed.

Figure 5 shows the streamline distribution in the air-cooling duct. As the figure shows, the streamline in the main air duct is disordered with many vortices. The enlarged drawing A shows cold air from the inlet directly entering No. 7 and No. 8 riser ducts, the resulting excessive airflow in the two riser ducts. Furthermore, when the air flows into a riser duct, it may shift to one side and rush to the bottom of the duct, increasing the airflow rate of the outlets at the bottom of the riser duct and decreasing the airflow rate of the outlets at the top of the riser duct. Moreover, when the air velocity is too high, a negative pressure zone is formed behind the outlets, resulting in a reverse flow phenomenon.

Table 4
Air velocity at the outlets (m/s)

Number of air outlet	Column number of air outlet									
	1	2	3	4	5	6	7	8	9	10
1	–3.17	–3.09	–4.23	–3.00	–3.51	–3.05	–2.93	–1.20	–2.83	–1.28
2	0.51	–0.90	0.20	–0.39	–0.40	–0.40	–0.61	–0.50	–0.93	0.47
3	1.12	1.02	0.68	1.01	0.06	0.58	0.01	0.66	0.38	0.96
4	1.54	1.61	1.59	1.78	0.89	1.64	0.97	2.22	0.72	1.16
5	2.05	2.15	2.01	2.12	1.47	2.39	2.05	2.75	1.33	1.96
6	2.57	2.82	2.95	2.55	2.23	2.99	2.98	3.20	2.01	2.38
7	3.28	3.45	4.15	3.14	3.40	3.37	3.35	4.10	2.80	2.93
8	4.07	4.46	2.71	3.83	4.50	4.65	3.70	0.68	3.19	3.39
9	4.67	2.42	0.99	4.66	2.98	2.51	1.07	0.87	0.16	0.88
10	3.19	2.42	4.55	3.33	3.03	2.96	2.43	4.13	3.00	2.73

Table 5
Air velocity at the outlets (m/s)

Number of air outlet	Column number of air outlet									
	11	12	13	14	15	16	17	18	19	20
1	–1.81	–0.42	–3.85	–0.75	–3.98	–4.22	–2.23	–3.51	–5.51	–4.48
2	–0.32	0.09	–1.05	0.76	0.36	–0.15	1.95	0.30	0.74	–1.91
3	0.71	–0.03	0.80	1.36	2.34	2.86	2.26	2.54	2.09	0.91
4	1.29	1.34	1.72	0.86	3.18	3.49	3.67	2.67	2.24	1.45
5	1.65	2.10	2.44	3.06	3.76	4.95	4.14	4.05	2.44	1.92
6	1.65	1.99	3.36	4.46	3.78	1.18	5.19	2.33	2.75	2.50
7	0.14	0.81	1.79	2.05	4.69	–0.60	1.65	–0.65	3.37	3.31
8	–0.41	0.65	0.20	0.58	5.87	–0.67	0.34	1.67	4.47	4.67
9	0.12	1.41	–0.28	2.70	1.67	2.44	2.13	3.35	5.66	5.31
10	2.05	2.05	3.88	4.96	3.73	5.95	5.46	6.23	6.04	5.48

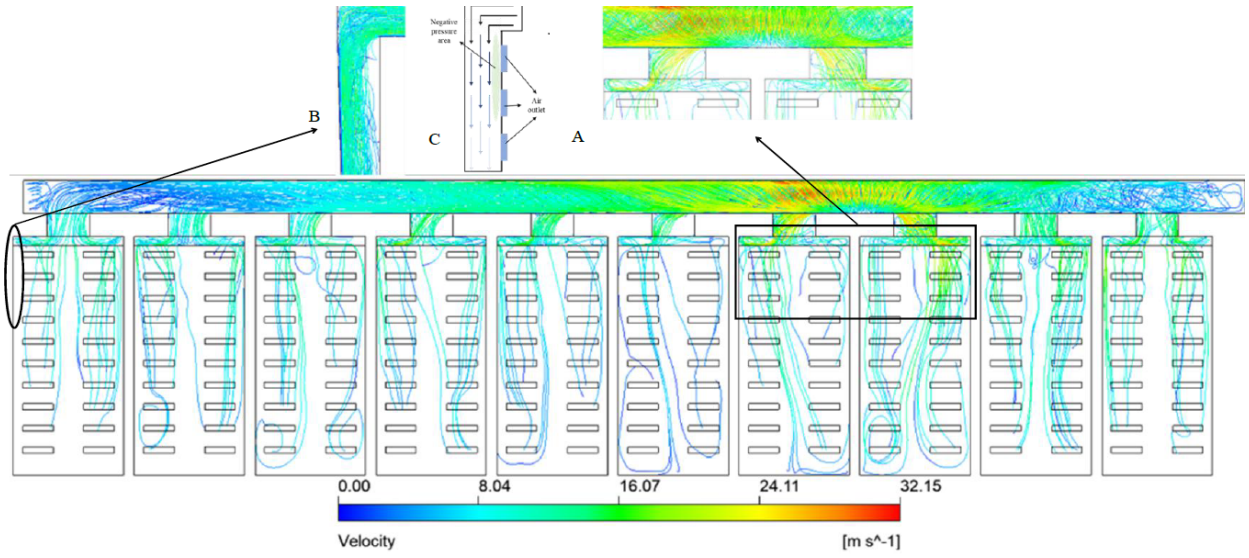

Fig. 5. Streamline distribution of the air-cooling duct

4.2. Optimization of the air-cooling duct structure

The air supply scheme should be optimized because of the problems of the initial air supply scheme in the previous section. The overall optimizing calculation is difficult with the complex structure. Therefore, this paper suggests that the main air duct and riser ducts are optimized separately. Figure 6 presents the optimization of the air-cooling duct. Firstly, the riser ducts are optimized by adopting a separated structure and installing baffles to make the air velocity at the outlets of each riser duct uniform. Secondly, the effect of the number and angle of the baffles on the uniformity of air velocity at the outlets is explored. Then, the optimized structure is obtained. Moreover, the optimization of the main air duct is simultaneous. In order to reduce the mutual interference between the air supply outlets, the air inlets are rearranged, and the cross-section of the main air duct is adjusted. Finally, the optimized main air duct is combined with the optimized riser ducts and the deflecting problem of combined airflow is corrected by the baffles at the entrance of the riser ducts.

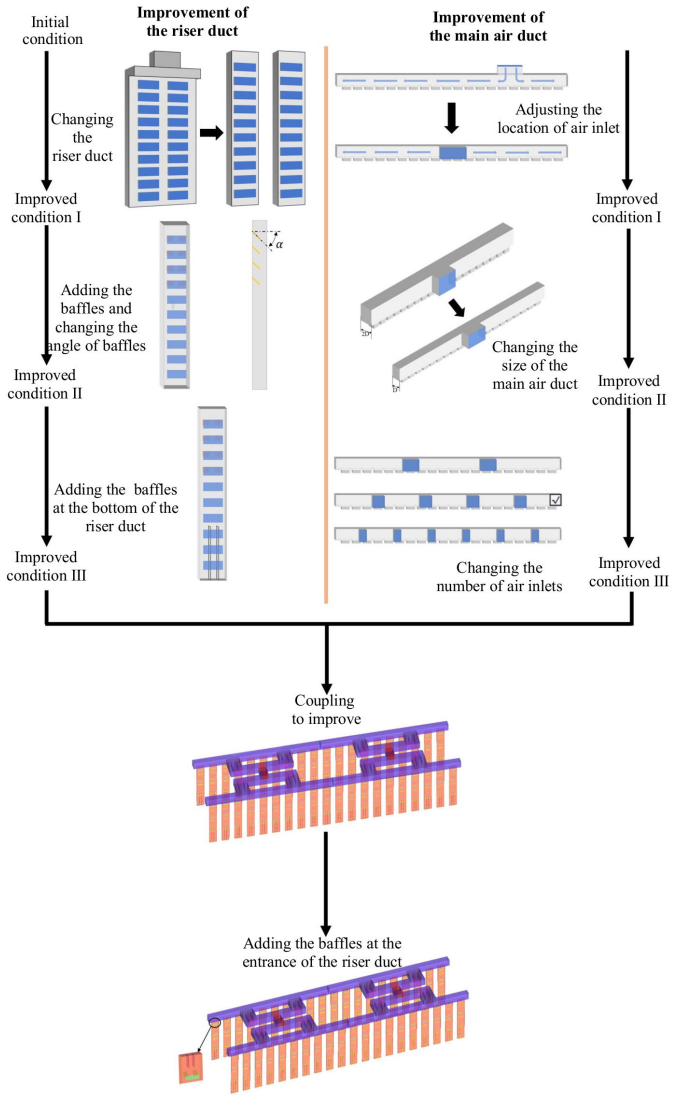

Fig. 6. Optimization of the air-cooling duct

4.2.1. Optimization of the riser duct structure

Controlling the airflow from the main air duct to each outlet of the riser duct is difficult when a riser duct is responsible for two rows of air outlets in the initial scheme. Therefore, the riser ducts are split into two parts, which are shown in Fig. 7.

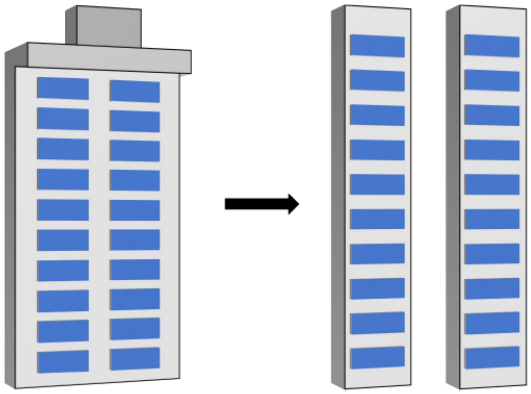

Fig. 7. Changes made to the riser duct structure

In order to adjust the inconsistent airflow rate of each outlet, some baffles are added to the riser duct, as is shown in Fig. 8. This section will first investigate the effect of the number and angle of the baffles on the uniformity of air velocity at the air outlets. Each baffle is 60×56 mm in size. Two baffles work as a group at each air outlet; α is the deflection angle of the baffle. The optimization scheme is shown in Table 6.

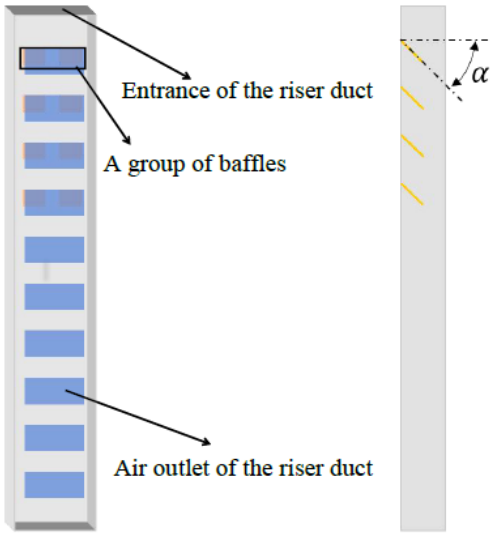

Fig. 8. Schematic diagram of the riser duct with the baffles installed

Figure 9 depicts the air velocity diagrams at the outlets of a riser duct for different baffle groups and angles.

As shown in Fig. 9, for a given baffle angle, the number of the baffles has little effect on the air velocity at the air outlets. When the baffle angle is 45°, the uniformity of the air velocity is significantly enhanced and is less affected by the change in

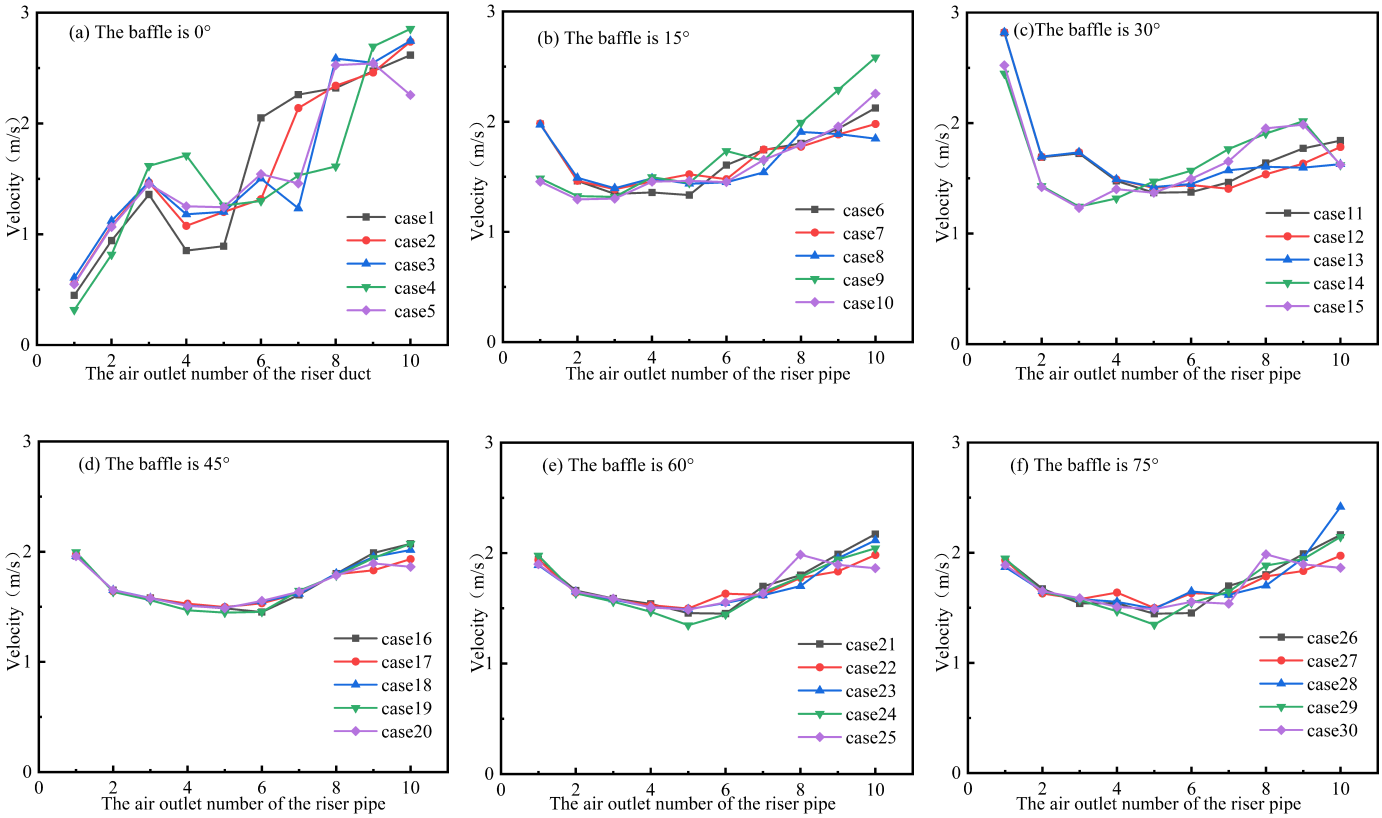

Fig. 9. Velocity diagrams of air at the air outlets of a riser duct for different baffle groups and angles

Table 6
Description of the riser duct optimization scheme

Angle of the baffle	Number of the baffle groups				
	4	5	6	7	8
0°	case1	case2	case3	case4	case5
15°	case6	case7	case8	case9	case10
30°	case11	case12	case13	case14	case15
45°	case16	case17	case18	case19	case20
60°	case21	case22	case23	case24	case25
75°	case26	case27	case28	case29	case30

the number of baffles. At the other baffle angles, the uniformity of air velocity at the outlet becomes worse than that at 45°. The velocity deviation coefficient is introduced to distinguish the air velocity uniformity in cases 15–20, which can be defined as follows:

$$L_i = \frac{|V_i - \overline{V}|}{\overline{V}}, \tag{2}$$

where V_i is the air velocity at the i-th air outlet, V is the average value of air velocity at the air outlets, and L_i is the velocity deviation coefficient.

Figure 10 shows the effect of the number of baffles on air velocity deviation coefficient (2%–25%) at ten outlets of the riser duct at a baffle angle of 45°. Case 20 is selected because its velocity deviation coefficient is the lowest among the five cases considered.

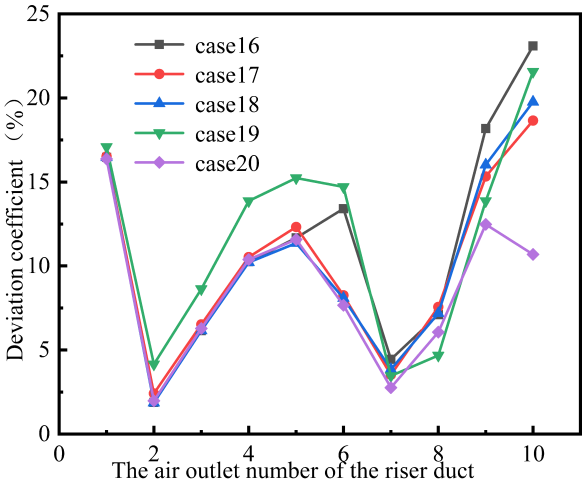

Fig. 10. Velocity deviation coefficient diagrams for a baffle angle of 45°

As the air flows to the bottom of the riser duct, it hits the bottom wall, causing bottom streamline disorder. Therefore, baffles are also installed at the bottom of the duct. The optimized riser duct is shown in Fig. 11.

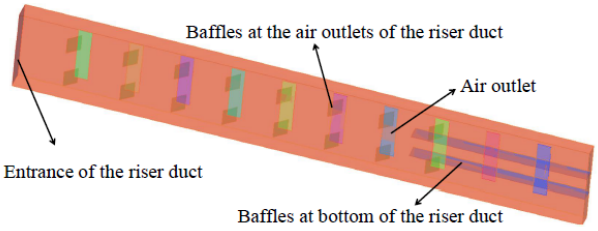

Fig. 11. Optimized riser duct

Figure 12 shows the air velocity diagrams at ten outlets of the optimized riser duct. It can be seen from the figure that at each air outlet, the air velocity is uniform (between 1.6 and 2.0 m/s).

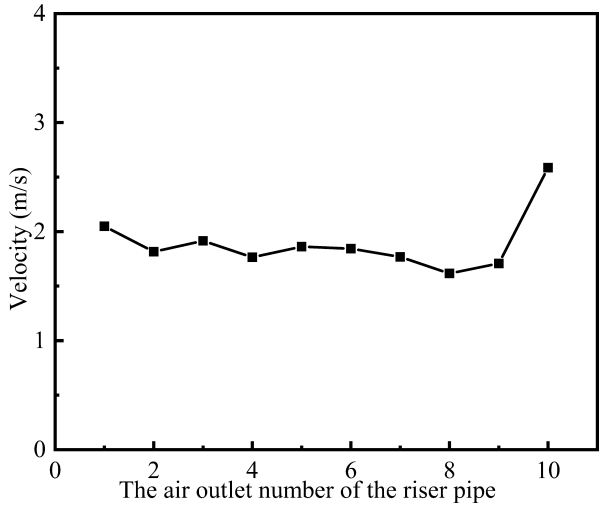

Fig. 12. Air velocity diagrams at the air outlets of the optimized riser duct

4.2.2. Optimization of the main air duct structure

The air supply from the upper right side of the main air duct is uneven. Therefore, the air inlet is shifted toward the middle of the main air duct, as shown in Fig. 13.

Besides, owing to the large size of the main air duct, streamlines are particularly prone to drift in the ducts. Therefore, the cross-section is reduced to improve the uniformity of the air velocity. Figure 14 is a schematic diagram showing the adjustment of the main air duct geometry.

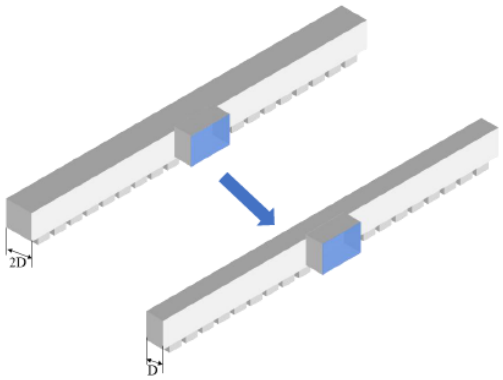

Fig. 14. Schematic diagram of the geometric adjustment of the main air duct

Figure 15 is the air velocity diagram of the outlets after adjusting the air inlets and duct structure. It can be seen from Fig. 15 that the air velocity in the main air duct is high in the middle and at both ends of the duct and that the air velocity at both sides is almost similar. Therefore, in this paper, the air velocity inconsistency of the main duct outlet is further alleviated by increasing the number of air supply inlets. Through consistent attempts, the four-inlet solution is proved to be superior.

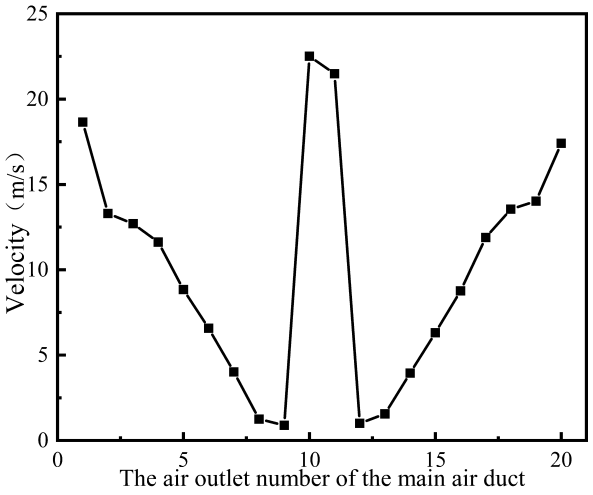

Fig. 15. Air velocity diagram of the outlets after adjusting the air inlets and duct structure

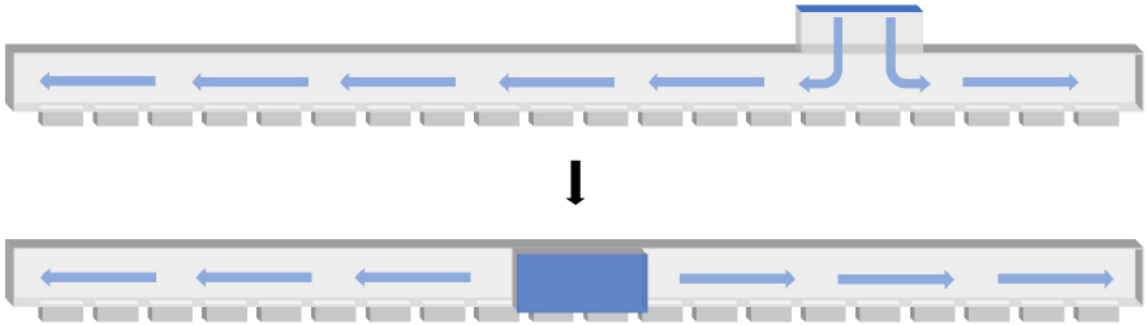

Fig. 13. Schematic diagram showing the air inlet position adjustment

The optimized main air duct is shown in Fig. 16. It has four air inlets on its side. Its width has been reduced, and an air duct with baffles has been installed between the duct and air supply box. The main duct is divided in the middle by a partition to reduce the mutual interference of the air supplies on the two sides.

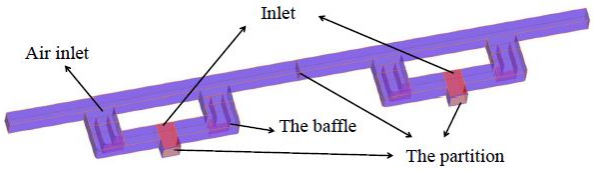

Fig. 16. Optimized main air duct

Figure 17 shows the air velocity diagram at the outlet of the optimized main air duct, the air velocity at the outlet of the main air duct is uniform after optimization and is in the 7.0–10.0 m/s range. According to formula (1), the nonuniformity coefficient of air velocity at the outlet of the main air duct is 0.065, and thus, an acceptable air supply scheme has been established after optimization.

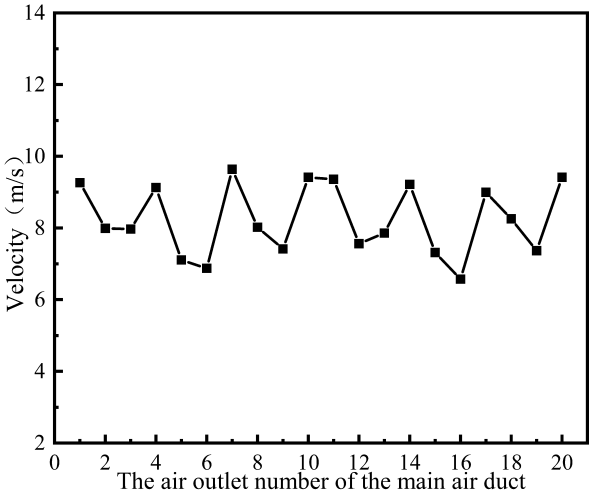

Fig. 17. Air velocity diagram at the outlet of the optimized main air duct

4.2.3. Optimization of the main air duct structure

After optimizing the main air duct and riser ducts, the optimized main air duct and the riser ducts should be combined, and the overall simulation calculation is performed. The overall model of the optimized air-cooling duct is shown in Fig. 18.

Figures 19 and 20 show the air streamlines and velocity nephograms at the air outlets of the optimized air-cooling duct.

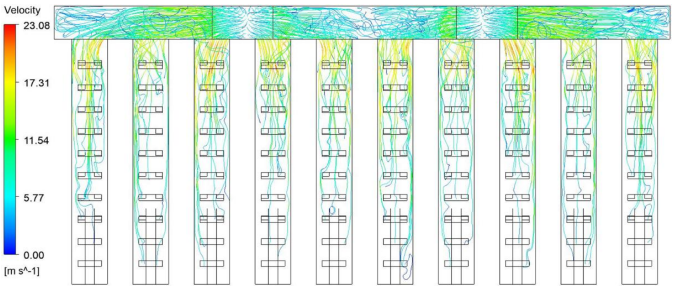

Fig. 19. Streamline distribution in the cooling duct after duct optimization

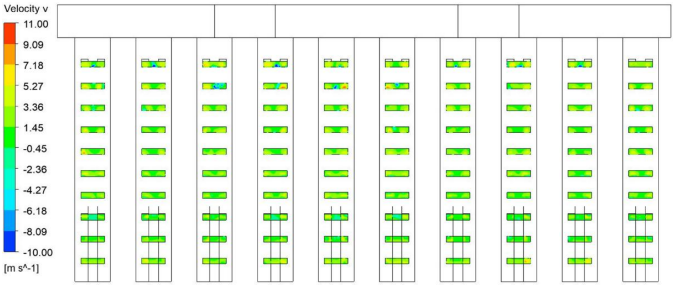

Fig. 20. Velocity nephogram in the cooling duct after duct optimization

As shown in Fig. 19, when the air flows into the riser duct through the main air duct, the airflow can get easily deflected to one side. It can be seen from Fig. 20 that the air velocity distribution at any air outlet is uneven, which is unfavorable for the heat dissipation of the battery. Therefore, baffles are installed at the entrance to the riser duct to improve the deflection of the airflow. Figure 21 is the schematic diagram of the air-cooling duct with baffles installed at the entrance to the riser ducts.

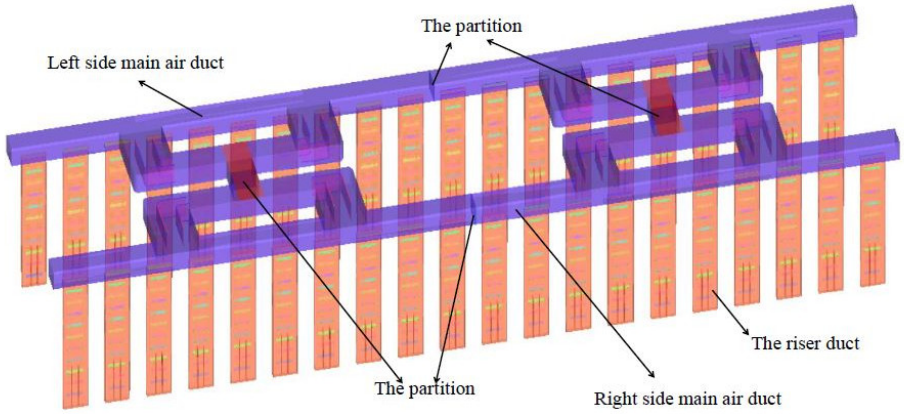

Fig. 18. Optimized air-cooling duct

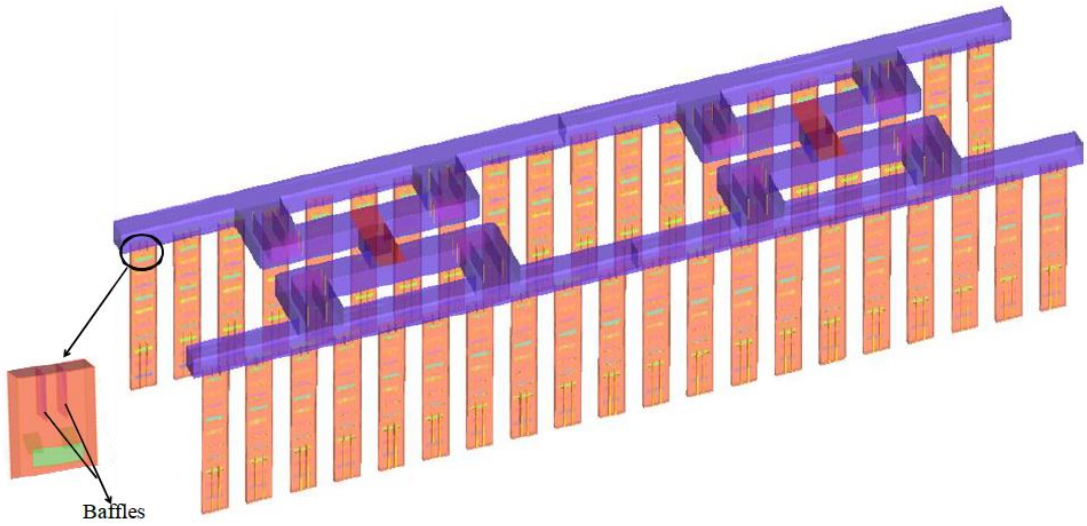

Fig. 21. Schematic diagram of the air-cooling duct with baffles installed at the entrance to the riser ducts

Figures 22 and 23 are the air streamline diagrams in the air-cooling duct and the air velocity nephogram at its air outlet after the baffles are installed at the entrance to each riser duct.

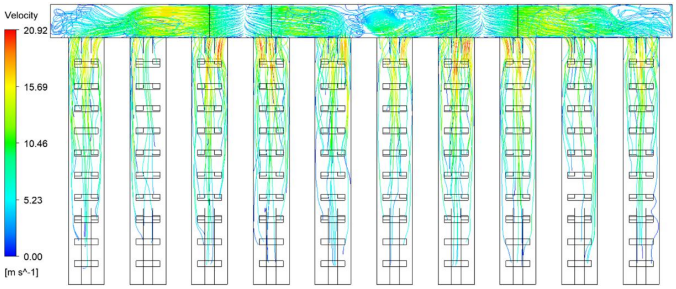

Fig. 22. Streamline diagram in the air-cooling duct after baffles have been installed at the entrances to the riser ducts

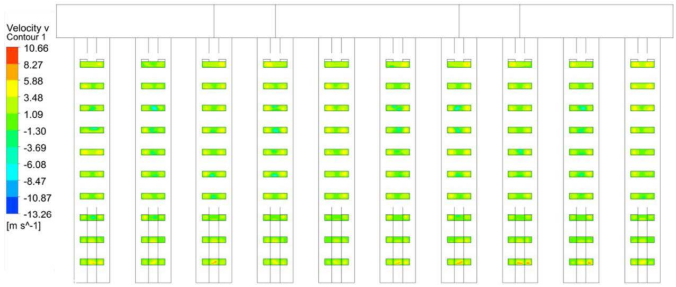

Fig. 23. Velocity nephogram at the air outlet of the air-cooling duct after baffles have been installed at the entrances to the riser ducts

It can be seen from Fig. 22 that air flows into the riser ducts through the main air duct with no deviation and that the airflow in each riser duct is smooth with no significant disturbance. And as shown in Fig. 23, the air velocities at the outlets of the cooling duct are uniform, with no significant differences existing among them.

4.2.4. Optimization of the main air duct structure

Table 7 shows the comparison of the main indexes of the air-cooling duct before and after its optimization.

Table 7
Comparison of the main indexes of the air-cooling duct before and after its optimization

	The velocity unevenness coefficient	Pressure loss (Pa)
Initial scheme	1.358	372.57
Optimization scheme	0.276	220.08

It can be seen from Table 7 that the nonuniformity coefficient of the air velocity has decreased from 1.358 to 0.276, and the uniformity of the air velocity at the air outlets has significantly improved. The pressure loss of air has decreased from 372.57 to 220.08 Pa. Therefore, the overall performance of the air-cooling duct has been significantly improved by optimization.

5. CONCLUSIONS

In this paper, an improved air supply scheme combining the main air duct and the riser ducts is designed for BESSs. The evaluation method of air supply uniformity is proposed and the ventilation system in each optimization process is simulated by the CFD method. The main findings listed in the paper are as follows:

1. The inhomogeneity of the outlet velocity of the riser duct is mainly caused by the inconsistency between the velocity direction of the airflow in the riser and the normal velocity at the outlet. And the airflow direction deviation and the airflow accumulation are also responsible for the inhomogeneity. The main method to solve the above problem is to add the baffles with inclination.
2. The inhomogeneity of the outlet velocity of the main air duct is mainly caused by the arrangement of the air inlets

and the duct section structure. A four-inlet solution has better performance. In terms of the uniformity of the air, reducing the cross-sectional area of the duct to double has also brought beneficial effects.

3. The uniformity of the airflow in the overall model can be effectively improved by installing baffles at the entrance to each riser duct. The nonuniformity coefficient of air velocity at the outlet of the air-cooling duct reduces from 1.358 to 0.276 with the optimization.

The personalized air supply scheme provided by this paper can effectively improve the comfort of the battery pack, restrain the excessive air supply, and ensure a compact structure.

REFERENCES

[1] Y. Shen, "Thermal analysis and optimization of container type energy storage system," *Electron. World*, no. 11, pp. 29–30, 2017.

[2] Ł. Nogal, S. Robak, and J. Bialek, "Advances in electrical power engineering," *Bull. Pol. Acad. Sci. Tech. Sci.*, vol. 68, no. 4, pp. 647–649, 2020, doi: 10.24425/bpasts.2020.134192.

[3] P. Komarnicki, "Energy storage systems: power grid and energy market use cases," *Arch. Electr. Eng.* ,vol. 65, no. 3, pp. 495–511, 2016, doi: 10.1515/aee-2016-0036.

[4] X. Xie, *et al.*, "Influencing factors of lithium-ion power battery safety," *Energy Storage Sci. Technol.*, vol. 6, no. 1, pp. 43-51, 2017, doi: 10.12028/j.issn.2095-4239.2016.0011.

[5] Y. Zhang, C. Wang, and X. Tang, "Cycling degradation of an automotive LiFePO4 lithium-ion battery," *J. Power Sources*, vol. 196, pp. 1513–1520, 2011, doi: 10.1016/j.jpowsour.2010.08.070.

[6] X. Feng, M. Ouyang, X. Liu, L. Lu, Y. Xia, and X. He, "Thermal runaway mechanism of lithium-ion battery for electric vehicles: A review," *Energy Storage Mater.*, vol. 10, pp. 246–267,2018, doi: 10.1016/j.ensm.2017.05.013.

[7] Q. Wang, P. Ping, X. Zhao, G. Chu, J. Sun, and C. Chen, "Thermal runaway caused fire and explosion of lithium-ion battery," *J. Power Sources*, vol. 208, no. 24, pp. 210–224, 2012, doi: 10.1016/j.jpowsour.2012.02.038.

[8] M. Klein, T. Song, and J. Park, "In-plane nonuniform temperature effects on the performance of a large-format lithium-ion pouch cell," *Appl. Energy*, vol. 165, pp. 639–647, 2016, doi: 10.1016/j.apenergy.2015.11.090.

[9] A. Pesaran, M. Keyser, G. Kim, S. Santhanagopalan, and K. Smith, "Tools for designing thermal management of batteries in electric drive vehicles," in *Advanced Automotive Battery Conference*, 2013 ,pp. 4–8, doi: 10.2172/1064502.

[10] P. Arora, R. White, and M. Doyle, "Capacity fade mechanisms and side reactions in lithium-ion batteries," *Cheminform*, vol. 29, pp. 3647–3667, 1998, doi: 10.1002/chin.199847297.

[11] B. Ziv, V. Borgel, D. Aurbach, J. Kim, X. Xiao, and B. Powell, "Investigation of the reasons for capacity fading in Li-ion battery cells batteries and energy storage," *J. Electrochem. Soc.*, vol. 161, pp. 1672–1680, 2014.

[12] J. Wang *et al.*, "Degradation of lithium ion batteries employing graphite negatives and nickel–cobalt–manganese oxide + spinel manganese oxide positives: part 1, aging mechanisms and life estimation," *J. Power Sources*, vol. 269, pp. 937–948, 2014, doi: 10.1016/j.jpowsour.2014.07.028.

[13] J. Jaguemont, L. Boulon, and Y. Dubé, "A comprehensive review of lithium-ion batteries used in hybrid and electric vehicles at cold temperatures," *Appl. Energy* ,164 ,pp. 99–114,2016, doi: 10.1016/j.apenergy.2015.11.034.

[14] Z. Rao and S. Wang, "A review of power battery thermal energy management," *Renew. Sust. Energ. Rev.*, vol. 15, pp. 4554–4571, 2011, doi: 10.1016/j.rser.2011.07.096.

[15] Z. Ling, F. Wang, X. Fang, X. Gao, and Z. Zhang, "A hybrid thermal management system for lithium ion batteries combining phase change materials with forced-air cooling," *Appl. Energy*, vol. 148, pp. 403–409, 2015, doi: 10.1016/j.apenergy.2015.03.080.

[16] L. Jin, P. Lee, X. Kong, Y. Fan, and S. Chou, "Ultra-thin minichannel LCP for EV battery thermal management," *Appl. Energy*, vol. 113, pp. 1786–1794, 2014, doi: 10.1016/j.apenergy.2013.07.013.

[17] Y. Huo, Z. Rao, X. Liu, and J. Zhao, "Investigation of power battery thermal management by using mini-channel cold plate," *Energy Conv. Manag.,* vol. 89, pp. 387–395, 2015, doi: 10.1016/j.enconman.2014.10.015.

[18] Z. Zhang, *et al.*, "Cooling and aseismicity study of the containerized energy storage systems," *Energy Storage Sci. Technol.*, vol. 2, no. 6, pp. 642–648, 2013, doi: 10.3969/j.issn.2095-4239.2013.06.012.

[19] L. Wang, *et al.*, "Thermal management structure design of lithium-ion battery pack for energy storage," *Power Supply Technol.*, vol. 35, no. 11, pp. 1351–1353,2011, doi: 10.3969/j.issn.1002-087X.2011.11.006.

[20] X. Wang, *et al.*, "Numerical simulation and optimization of container type energy storage system," *Energy Storage Sci. Technol.*, vol. 5, no. 4, pp. 577–582, 2016, doi: 10.12028/j.issn.2095-4239.2016.04.026.

[21] H. Sun, R. Dixon, "Development of cooling strategy for an air cooled lithium-ion battery pack," *J. Power Sources*, vol. 272, no. 25, pp. 404–414, 2014, doi: 10.1016/ j.jpowsour. 2014.08.107.

[22] Z. Lu *et al.*, "Parametric study of forced air cooling strategy for lithium-ion battery pack with staggered arrangement," *Appl. Therm. Eng.*, vol. 136, pp. 28–40, 2018, doi: 10.1016/j.applthermaleng.2018.02.080.

[23] Y. Liu, J. Zhang, "Design a J-type air-based battery thermal management system through surrogate-based optimization," *Appl. Energy*, vol. 252, p. 113426, 2019, doi: 10.1016/j.apenergy.2019.113426.

[24] B. Hba, *et al.*, "A new concept of thermal management system in li-ion battery using air cooling and heat pipe for electric vehicles," *Appl. Therm. Eng.*, vol. 174, p. 115280, 2020, doi: 10.1016/j.applthermaleng.2020.115280.

[25] H. Huang, H. Wang, J. Gu, and Y. Wu, "High-dimensional model representation-based global sensitivity analysis and the design of a novel thermal management system for lithium-ion batteries," *Energy Conv. Manag.*, vol. 190, pp. 54-72, 2019, doi: 10.1016/j.enconman.2019.04.013.

[26] Z. Yao, *et al.*, "Analysis and optimization of structural duct ventilation," *Mar. Technol.*, no. 5, pp. 82–88, 2016.